

Contents lists available at ScienceDirect

Journal of Energy Chemistry

journal homepage: www.elsevier.com/locate/jechem



http://www.journals.elsevier.com/

Letter

Modulating proton binding energy on the tungsten carbide nanowires surfaces for boosting hydrogen evolution in acid

Qingshui Hong ^{a,1}, Tangyi Li ^{a,1}, Shisheng Zheng ^a, Haibiao Chen ^a, Wenju Ren ^b, Honghao Chu ^a, Kuangda Xu ^a, Zongwei Mei ^a, Feng Pan ^{a,*}

ARTICLE INFO

Article history: Received 31 October 2020 Revised 25 March 2021 Accepted 5 April 2021 Available online 24 April 2021

Keywords: Carbon-encapsulated tungsten carbide Solid-state synthesis Self-supported nanoarrays electrode Hydrogen evolution reaction First-principles calculations

ABSTRACT

Tungsten carbides have attracted wide attentions as Pt substitute electrocatalysts for hydrogen evolution reaction (HER), due to their good stability in an acid environment and Pt-like behaviour in hydrolysis. However, quantum chemistry calculations predict that the strong tungsten-hydrogen bonding hinders hydrogen desorption and restricts the overall catalytic activity. Synergistic modulation of host and guest electronic interaction can change the local work function of a compound, and therefore, improve its electrocatalytic activity over either of the elements individually. Herein, we develop a creative and facile solid-state approach to synthesize self-supported carbon-encapsulated single-phase WC hybrid nanowires arrays (nanoarrays) as HER catalyst. The theoretical calculations reveal that carbon encapsulation modifies the Gibbs free energy of H* values for the WC adsorption sites, endowing a more favorable C@WC active site for HER. The experimental results exhibit that the hybrid WC nanoarrays possess remarkable Pt-like catalytic behavior, with superior activity and stability in an acidic media, which can be compared to the best non-noble metal catalysts reported to date for hydrogen evolution reaction. The present results and the facile synthesis method open up an exciting avenue for developing cost-effective catalysts with controllable morphology and functionality for scalable hydrogen generation and other carbide nanomaterials applicable to a range of electrocatalytic reactions.

© 2021 Science Press and Dalian Institute of Chemical Physics, Chinese Academy of Sciences. Published by ELSEVIER B.V. and Science Press. All rights reserved.

1. Introduction

Cost-effective manufacture of hydrogen gas as a green and renewable fuel source is one key component of the clean-energy technologies [1–4]. Electrochemical water splitting using electricity from sustainable energy sources (e.g., wind or solar) and non-Pt catalysts is an environmentally friendly and economically feasible scheme for large-scale hydrogen generation with advantages including zero carbon emission, high-purity product, and the ability to store intermittent renewable energy [5–7]. As a strongly uphill reaction, water splitting requires effective and low-cost catalysts for achieving the goal of a commercially viable hydrogen economy [8,9]. Despite recent extensive research to explore a variety of Pt-free materials as efficient electrocatalysts to accelerate the HER process (such as Co/MoS₂ [10], Co₂P/CoN [11], and Co/ β -

E-mail address: panfeng@pkusz.edu.cn (F. Pan).

Mo₂C@N-CNTs [12]), only a few candidates can satisfy the activity and durability requirements at the same time.

Tungsten carbides (WCs) have been considered as one of the most promising HER electrocatalysts because of their Pt-like dband density of states, high conductivity, tunable phase and electron configuration, as well as good physical and chemical stability [13-15]. Conventional strategies to produce WCs require tedious multi-step processes, rigorous reaction conditions (1400-1600 °C) and use of explosive gases such as CH₄ or CO as carbon sources [16–18]. The products usually suffer from the aggregation, particle coarsening, low surface area, poor morphology control, and the loss of active sites and catalytic performance, eventually hampering their widespread commercial application [19,20]. Another major limiting factor for pursuing higher performance is the strong bonding between hydrogen atoms and the WC surface, leading to favorable H+ reduction but restricted hydrogen desorption [21,22]. Generally, there are two effective approaches to address the above issues as follows: (i) nanostructure construction to provide a larger specific surface area and expose more active sites [23-25]; (ii) modulation of H-binding strengths by

^a School of Advanced Materials, Peking University, Shenzhen Graduate School, Shenzhen 518055, Guangdong, China

^b School of Advance Manufacturing Engineering, Chongqing University of Posts and Telecommunications, Chongqing 400065, China

^{*} Corresponding author.

¹ These authors contributed equally.

heteroatom doping [26], hetero-interface construction, [27] or optimizing the interfacial host-guest electronic interaction [28]. Nevertheless, it is a challenging task to develop a facile method without feeding a hydrocarbon gas for economical and scalable fabrication of highly dispersed and ultrafine WC nanocrystals with specific interfacial nanostructure and optimal surface binding energy for hydrogen.

Herein, we report a creative and facile solid-state synthesis pathway to obtain WC nanocrystals encapsulated in ultrathin carbon layers with vertically aligned nanowire structures on carbon fibres paper via in situ growth of W₁₈O₄₉ followed by a pyrolysis and carbonization process. Compared with conventional powdery electrocatalysts, the self-supported hybrid WC nanoarrays grown on the electrode not only exposes more active sites for HER process but also provides a low-resistance path suitable for fast electron transfer along the basal surfaces and simultaneously facilitates bubble formation and release from the electrode surface. As expected, the resulting materials offer Pt-like HER activity and stability in an acid media, outperforming the vast majority of reported WC-based catalysts. The density functional theory (DFT) calculation proves that the carbon-encapsulated shells induce a unique host-guest electronic interaction, weakening the H-binding energy of the WC interface, and thereby boost HER electrocatalytic activities.

2. Experimental

2.1. Synthesis of $W_{18}O_{49}$ nanoarrays on carbon fiber paper

 $W_{18}O_{49}$ nanowires were directly grown on a carbon fiber paper (CFP, 340 μm thick, resistivity <10 m Ω cm 2 , CeTech Co. Ltd.) by a solvothermal method [29]. Typically, 0.2 g tungsten (VI) chloride was dissolved in 100 mL absolute ethanol to form a slightly yellow precursor solution. Then, a piece of 1 \times 2 cm 2 CFP was immersed into the mixture and transferred to a Teflon-lined stainless steel autoclave. After heating the sealed autoclave at 180 °C for 24 h, the $W_{18}O_{49}$ nanowires on electrode was obtained and denoted as $W_{18}O_{49}$ –CFP. The sediment $W_{18}O_{49}$ powder was collected by filtration and washed with deionized water for 3 times.

2.2. Carbonization of $W_{18}O_{49}$ nanoarrays

The as prepared $W_{18}O_{49}$ –CFP was placed on the top of a combustion boat containing 2.0 g melamine at the base and heated to 900 °C for 2 hours at a heating rate of 5 °C min⁻¹ with Ar gas flowing in a tube furnace. After the carbonization process, the WC nanowires on electrode was obtained and denoted as WC–CFP. The WC powder was synthesized using the similar condition while $W_{18}O_{49}$ powder was used as the precursor. For comparison, the WC_(powder)–CFP electrode was obtained by dropping the WC powder ink (15 mg WC dispersed in 1 mL 5 wt% Nafion isopropanol solution) onto a CFP. The mass loading of catalysts on CFP is typically 1.2 mg cm⁻², and it was quite consistent from batch to batch.

2.3. Material characterizations

X–ray photoelectron spectra (XPS) were collected on a Thermo Fisher 250Xi X–ray photoelectron spectrometer at a pressure of about 2×10^{-9} Pa using Al $K\alpha$ X–rays as the excitation source. Raman scattering spectra (RSS) were recorded on a laser Raman microscope system (Renishaw inVia) with an excitation wavelength of 532 nm. The vibrational properties were analyzed by IR reflection spectroscopy using a Perkin-Elmer 1725X FTIR spectrometer. X–ray diffraction (XRD) patterns were collected on a Bruker D8 Advance X–ray diffractometer using a Cu K α source. The morphologies and compositions of the material were investigated on a transmission electron microscope (TEM, JEM–3200FS) equipped with energy dispersive X–ray spectroscopy and a scanning electron microscope (SEM, ZEISS SUPRA 55). The W₁₈O₄₉

and WC on the CFP were detached from the substrate by sonication for analysis.

2.4. Electrochemical tests

Electrochemical measurements were carried out in a standard three-electrode H-cell electrochemical system with a Nafion 211 membrane separator (DuPont) and controlled by an electrochemical workstation (Pine WaveDrive20). A platinum plate $(2 \times 2 \text{ cm}^2)$ and a saturated calomel electrode (SCE) were used as the counter and reference electrodes, respectively. The SCE was corrected with a reversible hydrogen electrode (RHE) and rinsed with deionized water before use. The catalyst-CFP was embedded into a carbon clip and used as the working electrode, with an active area of 1 cm² submerged in the electrolyte. A 0.5 M H₂SO₄ solution was used as the electrolyte, which was purged with argon for at least 60 min to ensure the removal of residual air in the reaction system. Commercial 10 wt% Pt/C (Alfa Aesar) was drop-casted onto CFP (Pt/C-CFP, 1.2 $mg_{Pt/C}$ cm⁻²) and measured as the HER benchmark. The cyclic voltammogram (CV) was firstly conducted at a scan rate of 50 mV s⁻¹ for twenty times to reach a relatively stable state. The electrochemical impedance spectroscopy (EIS) was tested from 10⁻¹ 3 to 10^5 Hz with amplitude of 10 mV at -0.35 V vs RHE. The electrochemical active surface area (ECSA) of the catalysts was evaluated by comparing the double-layer capacitance ($C_{\rm dl}$) within the non-Faradaic potential range at different scan rates of 20–120 mV s⁻¹. All linear sweep voltammetry (LSV) of the HER activity was conducted at a sweep rate of 10 mV s⁻¹. The Tafel slope was calculated according to Tafel equation as follows:

$\eta = b \cdot \log(j/j_0)$

where η denotes the overpotential, b denotes the Tafel slope, j denotes the current density, and j_0 denotes the exchange current density. The onset potentials were determined based on the beginning of the linear region in Tafel plots. The chrono-amperometry measurements were performed at different potentials.

2.5. Computational details

All the calculations were performed by means of spin-polarized DFT using Vienna ab initio simulation pack (VASP) with projector augmented wave (PAW) method [30]. A plane-wave cutoff energy of 450 eV was adopted and the Perdew-Burke-Ernzerhof (PBE) exchange-correlation functional was employed. To complement the deficiencies of DFT in dealing with dispersion interactions, DFT-D3 semi-empirical van der Waals corrections were included for structural optimization. For the calculation of Pt(111), $W_{18}O_{49}$ (010) and WC (100) slabs, a $3 \times 3 \times 1$ Monckhorst-Pack type kpoint grid was chosen. And the supercells consisting of $4 \times 4 \times 1$ unit cells were constructed, over which a vacuum space of at least 15 Å was used to separate the slabs. For the WC@C model, the p13 \times p13 supercell for graphene layers and the 3 \times 3 supercell for WC layers were applied. The Gibbs free energy in every elementary step was calculated by using the computational hydrogen electrode (CHE) model, which has been widely employed in the theoretical investigation of catalytic processes [12,31,32]. In this framework, the free energy of H^+/e^- pair is equivalent to the chemical potential of gaseous H_2 at standard conditions (pH = 0, P = 1 bar, T = 298.15 K). Accordingly, the free energy ΔG of each elemental step can be calculated as follows:

$$\Delta G = \Delta E + \Delta E_{ZPE} - T\Delta S + eU + k_B T \ln(10) \times pH$$

3. Results and discussion

The synthetic route of WC-CFP electrodes is schematically shown in Fig. 1a. W₁₈O₄₉ nanoarrays were first grown on CFP

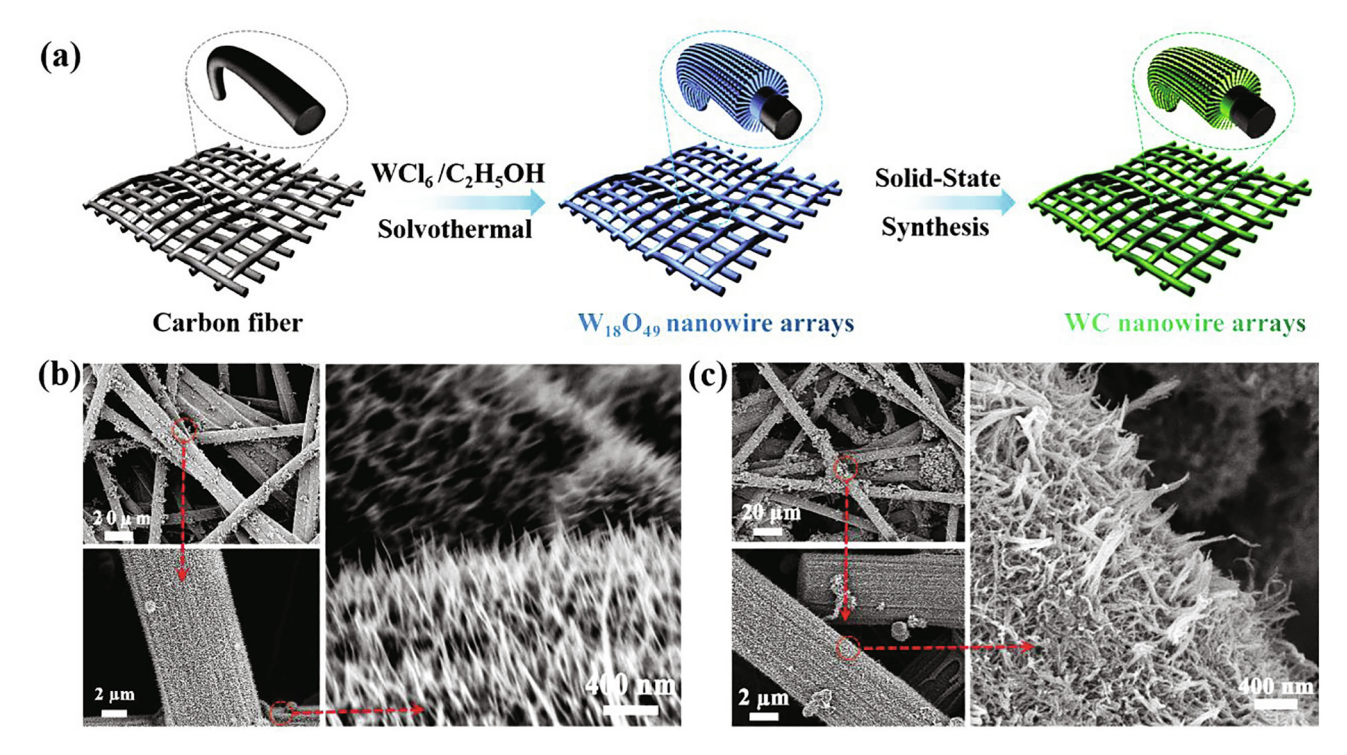


Fig. 1. (a) The schematic procedure of fabricating WC nanowire arrays on CFP. First, $W_{18}O_{49}$ nanoarrays were *in-situ* synthesized on CFP; then the $W_{18}O_{49}$ nanoarray was carbonized with melamine at high temperature by a facile solid-state synthesis strategy to obtain WC nanoarray. SEM of (b) $W_{18}O_{49}$ nanoarray and (c) WC nanoarray on CFP at different magnifications.

through a solvothermal reaction of WCl₆ in absolute ethanol. Afterwards, a subsequent solid-state reaction converted the nanoarrays to WC under Ar gas atmosphere at a high temperature, with using melamine powder as the carbon source. During the carbonization step, the CN_x species derived from melamine pyrolysis drove diffusion of carbon atoms into the W₁₈O₄₉ phase to form WC compound. The nitrogen left the sample completely as the carbonization temperature exceeded 800 °C (Fig. S6). SEM images in Fig. 1b show that vertically oriented W₁₈O₄₉ nanowires uniformly cover the surface of CFP. The morphology of $W_{18}O_{49}$ was well maintained after being converted to WC nanowires except for partial agglomerating into fascicular (Fig. 1c and Fig. S1). The length of the WC nanowires was determined to be about 1.1 μm (Fig. S1). This unique one-dimensional structure of nanowires not only provides highly active hydrogen binding sites during the HER process, but also facilitate electron transport along the basal surfaces [33-36].

Fig. 2a compares the XRD data of the $W_{18}O_{49}$ nanowires and their derived WC nanowires detached from CFP. The XRD pattern of W₁₈O₄₉ displays a monoclinic structure type (P2m) with sharp (010) and (020) peaks. This strongly suggests that the possible crystal growth direction of the nanowires is [010], which will be further confirmed by the direct observation of the high resolution transmission electron microscopy (HRTEM) image (Fig. S4). After carbonization, the original peaks were replaced by a series of new reflections at 31.5°, 35.6° and 48.3°, which correspond to the (001), (100) and (101) crystal planes of hexagonal WC phase, in accordance with the standard pattern (PDF#51-0939). Besides, the peak at 36.97° is consistent with the reflection of $WC_{1-x}(111)$ facet (PDF#20-1316), suggesting the existing of small amount of mixed phase in WC samples, which probably arises from the difference of carbon diffusion rate along the different crystal faces of nanowires during carbonization. The peak at 21.4° is the feature of graphitic carbon in the nanowires. X-ray photoelectron spectroscopy (XPS) was performed to get more insights on the chemical

environment of the WC nanowires. As shown in Fig. 2b, the survey scan of WC clearly revealed the presence of C, O and W. The atomic ratio between W and C was calculated to be 2.7:81. There was no N element detected on the surface of WC, which is consistent with EDS result in Fig. S6b. The high-resolution C 1s spectrum is displayed in Fig. 2c, which is mainly fit to C-W (283.4 eV), nonoxygenated C-C in the aromatic rings (285.3 eV) and C in C=O (287.5 eV). The presence of the C-W bond is also supported by the W 4f spectrum in Fig. 2d. Compared to W₁₈O₄₉ in Fig. S5b, the lower binding energy at 32.1 and 34.2 eV are supposed to be the W-C bonds, and the peaks centered at 35.6 and 37.9 eV are attributed to be the W-O bonds, resulting from the inevitable surface oxidation of WC upon exposure to air, which is consistent with Raman and FIIR results in Figs. S2 and 3, respectively [16]. The XPS results clearly demonstrate the successful carbonization of $W_{18} \\ O_{49}$ to WC phase by the solid-state synthesis method. The transmission electron microscopy (TEM) image in Fig. 2e shows a randomly entangled nanowires network structure for the WC after detached from the substrate. The derived carbide products maintain the morphology and structure except for a reduction in the diameter from about 7 nm for the $W_{18}O_{49}$ nanowires to about 3.5 nm. HRTEM image in Fig. 2f exhibits a hybrid nanowire structure of WC@C with plenty of ultrafine nanocrystals anchored within the continuous carbon supports, which may arise from the partial dissolution/precipitation of carbon from WC phase at a high temperature. The clear lattice fringes with an interplanar spacing of 0.251 nm for the nanocrystals correspond to the (100) plane of hexagonal WC. Elemental mapping images (Fig. 2g) show the homogenous distribution of C and W elements and the absence of N element in the WC nanowires. From the electrochemical point of view, such an elegant carbon encapsulated structure of the hybrid nanowire can be conducive to the efficient electron diffusion by improving the conductivity, achieving beneficial electronic states, synergistically reducing work function, and preventing the nanocrystals from coarsening and damage. Meanwhile, the nano-

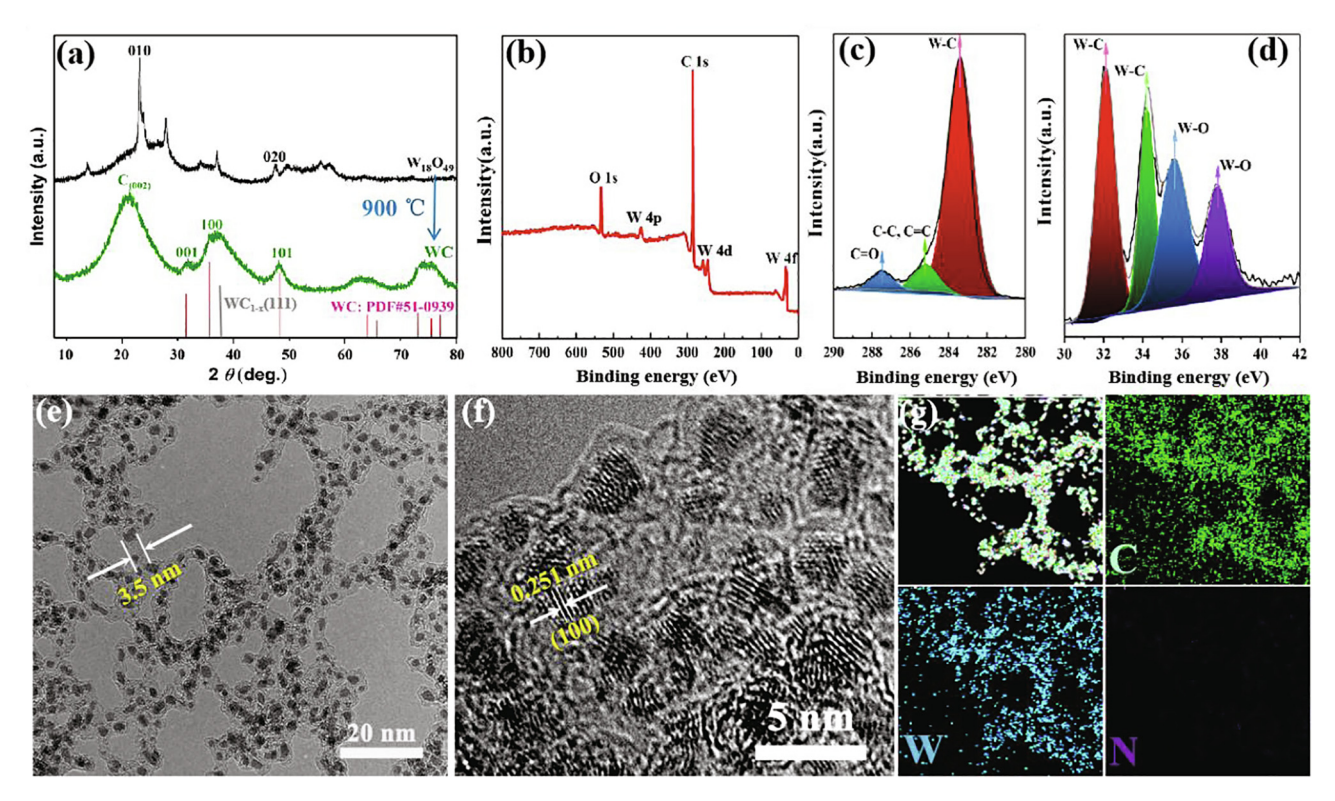


Fig. 2. (a) XRD pattern of the exfoliated W₁₈O₄₉ and WC. (b) XPS survey of the WC, and (c, d) high-resolution XPS of C 1 s and W 4f. (e-g) TEM, HRTEM and EDS mapping of the WC nanowires, respectively.

sized structure of the highly dispersed WC phase can offer abundant interfaces and active sites, and all of these features benefit the HER [37–39].

The electrocatalytic performance of WC nanoarrays on electrode for HER was measured in 0.5 M H₂SO₄. Fig. 3a displays the LSV curves on the reversible hydrogen electrode scale of the vari-

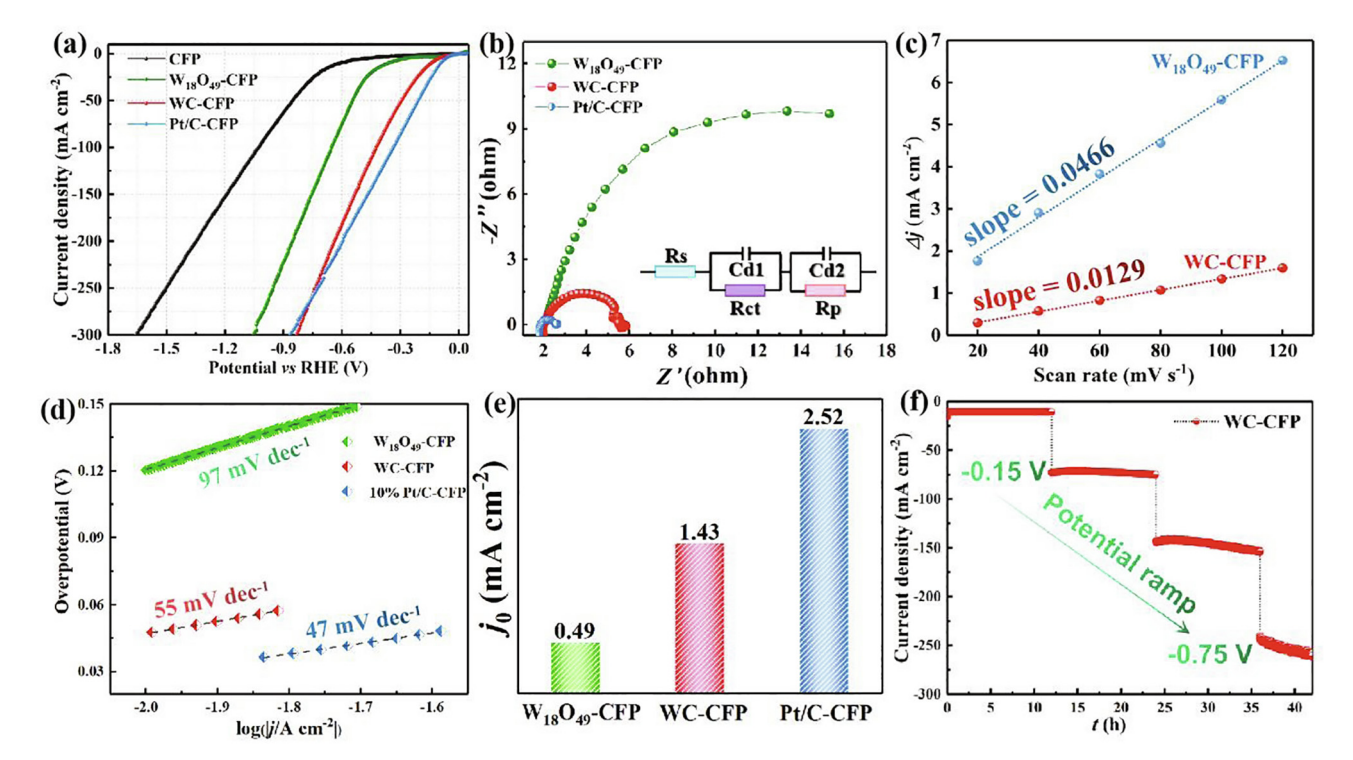


Fig. 3. (a) LSVs of CFP, $W_{18}O_{49}$ -CFP, WC-CFP and Pt/C-CFP in 0.5 M H_2SO_4 with iR correction at 10 mV s⁻¹. (b) EIS spectra of $W_{18}O_{49}$ -CFP, WC-CFP and Pt/C-CFP and the inset shows the equivalent circuit used for fitting the Nyquist plots. (c) Capacitive current at 0.5 V vs RHE as a function of scan rates for $W_{18}O_{49}$ -CFP, WC-CFP and Pt/C-CFP with supply voltages varying from -0.15 to -0.75 V vs RHE.

ous compared electrodes with iR correction. The WC-CFP electrode exhibits catalytic performance with an overpotential of -152 mV at -10 mA cm^{-2} and -417 mV at -100 mA cm^{-2} , which is smaller than that of the bare CFP and W₁₈O₄₉-CFP and comparable to the Pt/C benchmark catalyst usually used (see Tables S1, S2). The fast HER reaction kinetics of WC-CFP is also demonstrated by the results of EIS with a small charge transfer resistance of 3.17 ohms at the potential of -0.35 V vs RHE (Fig. 3b), which are in good agreement with their LSV behavior. After high temperature carbonization, the WC-CFP showed a decreased ECSA than that of W₁₈O₄₉-CFP (estimated from the electrochemical double layer capacitance of the catalysts, Fig. 3c and S7), which could be ascribed to the partial agglomeration of the slender WC nanowires. The corresponding Tafel slope of WC-CFP was 55 mV dec⁻¹, closed to the commercial 10% Pt/C (47 mV dec⁻¹), indicating a favorable HER kinetics (Fig. 3d). Moreover, the exchanged current density (i_0) obtained by extrapolation to the Tafel plots (Fig. 3e) reflects the intrinsic catalytic activity. The exchanged current density of the WC-CFP (1.43 mA cm⁻²) is as high as that of Pt/C benchmark (2.52 mA cm⁻²), which implies favorable HER kinetics at the WC-CFP electrolyte interface. In addition, the WC-CFP showed much higher activity than its powder counterparts (Fig. S9 and Table S3), which implies that the self-supported structure favors HER. Thanks to the elegant self-supported nanoarray structure, the WC-CFP could both guarantee more active sites for electrochemical reaction and also facilitate gas evolution at the neat and free standing catalytic surfaces. Other than activity, the stability is another key parameter for high-performance HER electrodes, as it determines the cycle life of the electrodes during practical applications. As shown in Fig. 3f, long-time chrono-amperometric (CA) measurement was used to investigate the durability of the WC-CFP at various constant overpotential from -0.15 to -0.75 V vs RHE (12 h for every plateau), which presents stable current density over 36 h at low overpotentials (less than -0.55 V vs RHE), and only a slight improvement at the high overpotential of -0.75 V vs RHE, which may arise from the less accumulation and rapid releases of bubble on the electrode under fast reaction rates. As another piece of evidence, Fig. 4a further confirms the remarkable stability of the WC-CFP in the acidic electrolyte, in which the electrode provides similar polarization curves before and after longterm test, with the maximum difference in overpotential (Δn) as small as 15 mV at the current density of 48 mA cm⁻². This high durability of the WC samples were also verified by the XRD, XPS and HRTEM characterizations after HER cycles, as shown in

To further provide atomic level understandings of the high electrocatalytic activity of such hybrid nanowires towards the HER, we calculated the detailed energy profiles of HER pathways. Based on the TEM results of the hybrid WC nanowires, we use the correlative theoretical model WC@C with carbon layer covering the (100) sur-

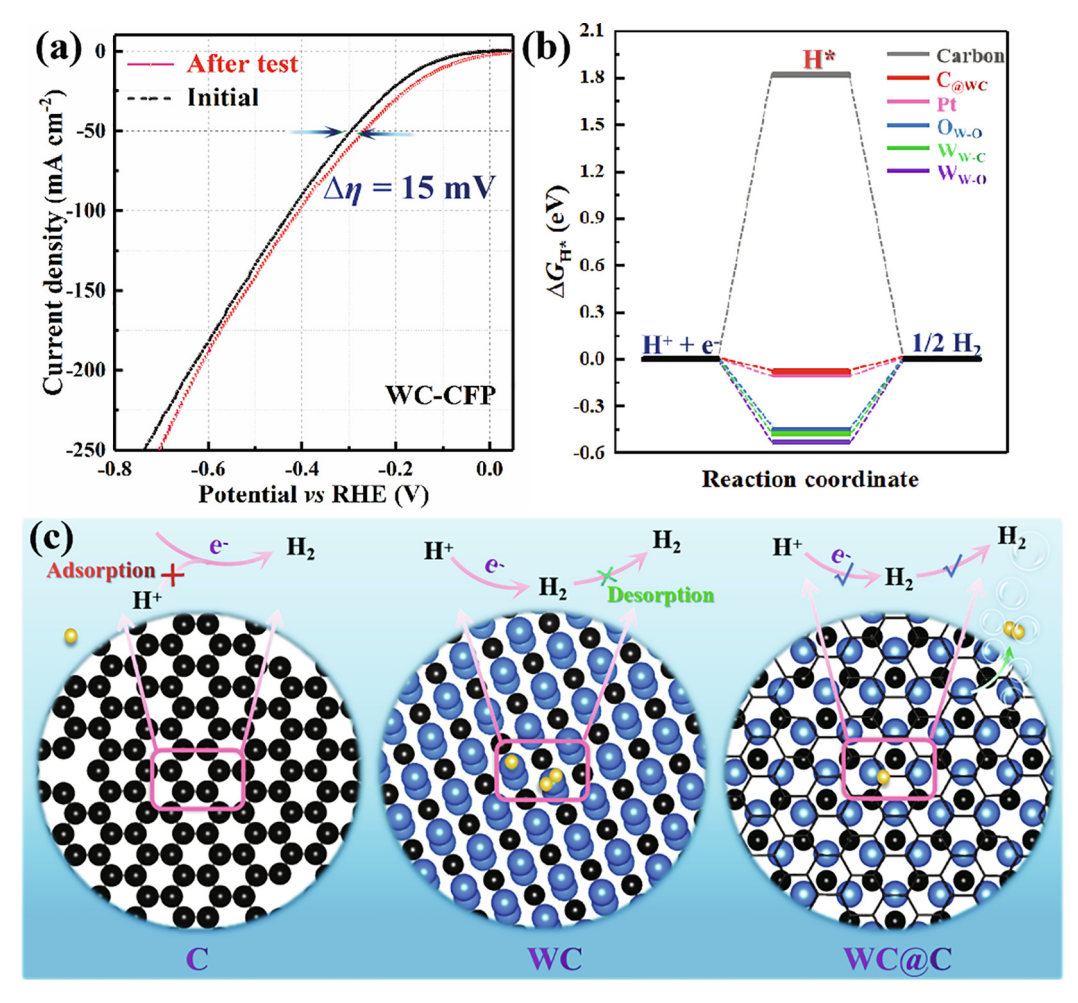


Fig. 4. (a) LSV curves of WC-CFP initially and after long time step chronoamperometry measurement. The maximum value of difference overpotential ($\Delta\eta$) is as small as 15 mV at the current density of 48 mA cm⁻². (b) The computed Gibbs free energies of H* values for the adsorption sites on the WC@C model, the sole WC, W₁₈O₄₉ and the graphitized carbon, as well as Pt as a benchmark. (c) Schematic illustration of the HER process catalyzed by carbon, WC and WC@C materials, in which the blue, black and yellow spheres denote the W, C and H, respectively, and the hexatomic rings denote the carbon layer covered over the WC surface.

face of WC to construct the DFT calculations, as shown in the inset of Fig. 4b. Regarding the overall HER rate, it is generally accepted that the HER activity closely correlates with the adsorption energy of a single H atom (ΔG_{H^*}), for which the optimal HER catalysts should have ΔG_{H^*} close to zero. For comparison, five representative adsorption sites of H* are sampled as the studied models (Fig. 4b), including the carbon atoms over the WC, the W sites in WC crystal lattice, the W and O atom sites in $W_{18}O_{49}$ crystal lattice and the graphitized carbon sites, which were denoted as C_{@W-C}, W_{W-C}, W_{W-O}, O_{W-O} and carbon, respectively. The computational results revealed that the W_{W-C} , W_{W-O} and O_{W-O} sites possess aggressively negative ΔG_{H^*} of -0.45, -0.53 and -0.48 eV, respectively. On the other hand, the pure carbon sites exhibit complete opposite ΔG_{H^*} value. Interestingly, the hybrid WC@C structure with integrated WC sites and carbon layer shows a very low ΔG_{H^*} value of only -0.077 eV on the $C_{\omega W-C}$ site, which is near zero and similar to that of Pt (-0.092 eV). It can be concluded that the $C_{@W-C}$ sites could be the favorable active site and possess considerably high HER catalytic activity, owing to the unique host guest electronic synergistic interaction between WC and carbon layer. According to previous report, this interaction can actually activate the C atoms in the carbon layer and effectively change the local work function of the carbon layers toward HER [28,40–42], endowing the surface of hybrid WC@C with excellent HER activity that is superior to most of WC based catalysts recently reported and also outstanding among the most active HER electrocatalysts in acid, as shown in Fig. S11 and Table S5. It is noted that the larger Tafel slope of WC@C than that of Pt catalyst may result from the presence of W_{W-C} , W_{W-O} and O_{W-O} sites in WC@C structure.

Given the discussions above, the enhancement of HER by modulating proton binding energy is proposed and illustrated in Fig. 4c. For the pure carbon materials, despite of an excellent electronic conductivity, their ΔG_{H^*} is endothermic with high uphill value of 1.82 eV, indicating that the surface of pure carbon is unfavourable for proton trapping and leads to a large onset overpotential for HER. Conversely, the protons bind strongly to WC, which favors protons adsorption and reduction but hinders hydrogen desorption. Interestingly, when WC supercells bond with carbon shells, the surface ΔG_{H^*} value of WC@C is sharply reduced to close to zero, suggesting that the synergistic interfacial electronic configuration between WC and C phases could regulate the proton binding strength and tremendously promote HER catalytic activity. Consequently, the as-obtained WC@C nanoarrays electrocatalysts make full use of the improvement effect on the HER performance by rich one-dimensional WC@C interfaces with moderate proton binding strength, giving rise to the best electrocatalytic performance.

4. Conclusions

In summary, we developed a facile solid-state synthesis strategy for controlled synthesis of vertically aligned as efficient and robust catalyst for HER in acid electrolytes. The SEM, XRD and TEM investigation verified that the ultrafine WC nanocrystals are well confined in the hybrid WC@C nanowires, revealing the effectiveness of synthesis method. DFT calculations revealed that the synergistic electronic effect between WC and its carbonencapsulated shells greatly optimized the H-binding energy, thereby boosting HER electrocatalytic activities. Due to the unique synergetic WC@C structure with rich one-dimensional activated carbon layers interfaces and a high content of active sites, the resulting hybrid nanoarrays exhibited remarkable HER catalytic activity associated with long-term stability, making the hybrid WC nanoarrays a promising alternative nonprecious HER electrocatalyst. This work may open up new avenues for developing and tailoring novel interface with synergistic electronic effect and

exploring the next generation of nonprecious electrocatalysts as well as potential uses in other technological systems.

Declaration of competing interest

The authors declare that they have no known competing financial interests or personal relationships that could have appeared to influence the work reported in this paper.

Acknowledgments

This work was supported by the Shenzhen Science and Technology Research Grant (ZDSYS201707281026184) and the Natural Science Foundation of Shenzhen (JCYJ20190813110605381).

Appendix A. Supplementary data

Supplementary data to this article can be found online at https://doi.org/10.1016/j.jechem.2021.04.004.

References

- [1] X. Tian, P. Zhao, W. Sheng, Adv. Mater. 31 (2019) 1808066.
- [2] Y. Chen, R. Ren, Z. Wen, S. Ci, J. Chang, S. Mao, J. Chen, Nano Energy 47 (2018) 66–73.
- [3] C.J. Lei, Y. Wang, Y. Hou, P. Liu, J. Yang, T. Zhang, X.D. Zhuang, M.W. Chen, B. Yang, L.C. Lei, C. Yuan, M. Qiu, X.L. Feng, Energ, Environ. Sci. 12 (2019) 149–156
- [4] Y. Guo, B. Chang, T. Wen, S. Zhang, M. Zeng, N. Hu, Y. Su, Z. Yan, B. Yang, J. Colloid Interf. Sci. 567 (2020) 213–223.
- [5] Z.H. Pu, J.H. Zhao, I.S. Amiinu, W.Q. Li, M. Wang, D.P. He, S.C. Mu, Energy Environ. Sci. 12 (2019) 952–957.
- [6] R. Koutauarapu, C.V. Reddy, B. Babu, K.R. Reddy, M. Cho, J. Shim, Int. J. Hydrogen Energy 45 (2020) 7716–7740.
- [7] S.Y. Jing, L.S. Zhang, L. Luo, J.J. Lu, S.B. Yin, P.K. Shen, P. Tsiakaras, Appl. Catal. B-Environ. 224 (2018) 533–540.
- [8] J.Y. Xu, T.F. Liu, J.J. Li, B. Li, Y.F. Liu, B.S. Zhang, D.H. Xiong, I. Amorim, W. Li, L.F. Liu, Energy Environ. Sci. 11 (2018) 1819–1827.
- [9] J.-Q. Chi, M. Yang, Y.-M. Chai, Z. Yang, L. Wang, B. Dong, J. Energy Chem. 48 (2020) 398–423.
- [10] Q.Z. Xiong, Y. Wang, P.F. Liu, L.R. Zheng, G.Z. Wang, H.G. Yang, P.K. Wong, H.M. Zhang, H.J. Zhao, Adv. Mater. 30 (2018) 1801450.
- [11] Y.Y. Guo, P.F. Yuan, J.A. Zhang, H.C. Xia, F.Y. Cheng, M.F. Zhou, J. Li, Y.Y. Qiao, S. C. Mu, Q. Xu, Adv. Funct. Mater. 28 (2018) 1805641.
- [12] T. Ouyang, Y.Q. Ye, C.Y. Wu, K. Xiao, Z.Q. Liu, Angew. Chem. Int. Ed. 58 (2019) 4923–4928.
- [13] X. Wei, N. Li, Appl. Surf. Sci. 463 (2019) 1154–1160.
- [14] H. Jin, J. Chen, S. Mao, Y. Wang, ACS Appl. Mater. Inter. 10 (2018) 22094– 22101.
- [15] X. Chen, S. Li, X. Sun, F. Liu, C. Li, J. Yu, S. Mu, Electrochim. ACTA 328 (2019) 135077.
- [16] Q. Feng, Y. Xiong, L. Xie, Z. Zhang, X. Lu, Y. Wang, X.-Z. Yuan, J. Fan, H. Li, H. Wang, ACS Appl. Mater. Inter. 11 (2019) 25123–25132.
- [17] S. Emin, C. Altinkaya, A. Semerci, H. Okuyucu, A. Yildiz, P. Stefanov, Appl. Catal. B-Environ. 236 (2018) 147–153.
- [18] Y. Yan, L. Zhang, X. Qi, H. Song, J.-Y. Wang, H. Zhang, X. Wang, Small. 8 (2012) 3350–3356.
- [19] D. Zhu, M. Qiao, J. Liu, T. Tao, C. Guo, J. Mater. Chem. A 8 (2020) 8143-8170.
- [20] C. Huang, T. Ouyang, Y. Zou, N. Li, Z.Q. Liu, J. Mater. Chem. A 6 (2018) 7420–7427.
- [21] J. Chen, B. Ren, H. Cui, C. Wang, Small 16 (2020) 1907556.
- [22] Z. Kou, T. Wang, H. Wu, L. Zheng, S. Mu, Z. Pan, Z. Lyu, W. Zang, S.J. Pennycook, J. Wang, Small 15 (2019) 1900248.
- [23] Z.H. Li, M.F. Shao, L. Zhou, R.K. Zhang, C. Zhang, M. Wei, D.G. Evans, X. Duan, Adv. Mater. 28 (2016) 2337–2344.
- [24] S. Tan, B.M. Tackett, Q. He, J.H. Lee, J.G. Chen, S.S. Wong, Nano Res. 13 (2020) 1434–1443.
- [25] Z. Chen, W. Gong, S. Cong, Z. Wang, G. Song, T. Pan, X. Tang, J. Chen, W. Lu, Z. Zhao, Nano Energy 68 (2020) 104335.
- [26] N.N. Han, K.R. Yang, Z.Y. Lu, Y.J. Li, W.W. Xu, T.F. Gao, Z. Cai, Y. Zhang, V.S. Batista, W. Liu, X.M. Sun, Nat. Commun. 9 (2018) 10.
 [27] J. Diao, Y. Qiu, S. Liu, W. Wang, K. Chen, H. Li, W. Yuan, Y. Qu, X. Guo, Adv.
- Mater. 32 (2020) 1905679. [28] S. Jing, J. Lu, G. Yu, S. Yin, L. Luo, Z. Zhang, Y. Ma, W. Chen, P.K. Shen, Adv. Mater.
- [28] S. Jing, J. Lu, G. Yu, S. Yin, L. Luo, Z. Zhang, Y. Ma, W. Chen, P.K. Shen, Adv. Mater 30 (2018) 1705979.
- [29] Y. Tong, H. Guo, D. Liu, X. Yan, P. Su, J. Liang, S. Zhou, J. Liu, G.Q. Lu, S.X. Dou, Angew. Chem. Int. Ed. 59 (2020) 7356–7361.
- [30] P.E. Blochl, Phys. Rev. B 50 (1994) 17953-17979.

- [31] C.L. Tan, Z.M. Luo, A. Chaturvedi, Y.Q. Cai, Y.H. Du, Y. Gong, Y. Huang, Z.C. Lai, X. Zhang, L.R. Zheng, X.Y. Qi, M.H. Goh, J. Wang, S.K. Han, X.J. Wu, L. Gu, C. Kloc, H. Zhang, Adv. Mater. 30 (2018) 1705509.
- [32] N. Ran, W. Qiu, E. Song, Y. Wang, X. Zhao, Z. Liu, J. Liu, Chem. Mater. 32 (2020) 1224-1234.
- [33] Y. Zhu, G. Chen, Y. Zhong, W. Zhou, Z. Shao, Adv. Sci. 5 (2018) 1700603.
 [34] H.M. Sun, Z.H. Yan, F.M. Liu, W.C. Xu, F.Y. Cheng, J. Chen, Adv. Mater. 32 (2020) 1806326.
- [35] Y.B. Li, Y. Bando, D. Golberg, Adv. Mater. 15 (2003) 1294–1296.
- [36] M.Q. Wang, C. Ye, H. Liu, M.W. Xu, S.J. Bao, Angew. Chem. Int. Ed. 57 (2018) 1963-1967.
- [37] G. Nam, J. Park, M. Choi, P. Oh, S. Park, M.G. Kim, N. Park, J. Cho, J.S. Lee, ACS Nano 9 (2015) 6493-6501.
- [38] M. Chu, L. Wang, X. Li, M. Hou, N. Li, Y. Dong, X. Li, Z. Xie, Y. Lin, W. Cai, C. Zhang, Electrochim. ACTA 264 (2018) 284-291.
- [39] X.J. Wei, Y.H. Zhang, H.C. He, D. Gao, J.R. Hu, H.R. Peng, L. Peng, S.H. Xiao, P. Xiao, Chem. Commun. 55 (2019) 6515-6518.
- [40] I. Shanenkov, A. Ivashutenko, Y. Shanenkova, D. Nikitin, Y. Zhu, J. Li, W. Han, A. Sivkov, J. Alloy. Compd. 834 (2020) 155116.
- [41] X.J. Fan, Z.W. Peng, R.Q. Ye, H.Q. Zhou, X. Guo, ACS Nano 9 (2015) 7407-7418.
- [42] X.F. Lu, L. Yu, J. Zhang, X.W. Lou, Adv. Mater. 31 (2019) 1900699.